Near Infrared Autofluorescence Lifetime Imaging of Human Retinal Pigment Epithelium Using Adaptive Optics Scanning Light Ophthalmoscopy

Karteek Kunala,[1,2] Janet A. H. Tang,[1,3] Kristen E. Bowles Johnson,[1,4,5] Khang T. Huynh,[1,6,7] Keith Parkins,[1] Hye-Jin Kim,[8,9] Qiang Yang,[1] Janet R. Sparrow,[9] and Jennifer J. Hunter[1,4,10]

[1]Center for Visual Science, University of Rochester, Rochester, New York, United States
[2]Byers Eye Institute, Stanford University, Palo Alto, California, United States
[3]The Institute of Optics, University of Rochester, Rochester, New York, United States
[4]Flaum Eye Institute, University of Rochester, Rochester, New York, United States
[5]School of Optometry, Indiana University, Bloomington, Indiana, United States
[6]Department of Biomedical Engineering, University of Rochester, Rochester, New York, United States
[7]Herbert Wertheim School of Optometry & Vision Science, University of California, Berkeley, Berkeley, California, United States
[8]College of Pharmacy, Keimyung University, Dalseo-gu, Daegu, South Korea
[9]Department of Ophthalmology, Columbia University Medical Center, New York, New York, United States
[10]School of Optometry and Vision Science, University of Waterloo, Waterloo, Ontario, Canada

Correspondence: Karteek Kunala, 2370 Watson Ct, Palo Alto, CA 94303, USA; kkunala@stanford.edu.

Received: August 7, 2023
Accepted: April 23, 2024
Published: May 17, 2024

Citation: Kunala K, Tang JAH, Bowles Johnson KE, et al. Near infrared autofluorescence lifetime imaging of human retinal pigment epithelium using adaptive optics scanning light ophthalmoscopy. *Invest Ophthalmol Vis Sci.* 2024;65(5):27. https://doi.org/10.1167/iovs.65.5.27

Purpose. To demonstrate the first near-infrared adaptive optics fluorescence lifetime imaging ophthalmoscopy (NIR-AOFLIO) measurements in vivo of the human retinal pigment epithelial (RPE) cellular mosaic and to visualize lifetime changes at different retinal eccentricities.

Methods. NIR reflectance and autofluorescence were captured using a custom adaptive optics scanning light ophthalmoscope in 10 healthy subjects (23–64 years old) at seven eccentricities and in two eyes with retinal abnormalities. Repeatability was assessed across two visits up to 8 weeks apart. Endogenous retinal fluorophores and hydrophobic whole retinal extracts of *Abca4*$^{-/-}$ pigmented and albino mice were imaged to probe the fluorescence origin of NIR-AOFLIO.

Results. The RPE mosaic was resolved at all locations in five of seven younger subjects (<35 years old). The mean lifetime across near-peripheral regions (8° and 12°) was longer compared to near-foveal regions (0° and 2°). Repeatability across two visits showed moderate to excellent correlation (intraclass correlation: 0.88 [τ_m], 0.75 [τ_1], 0.65 [τ_2], 0.98 [a_1]). The mean lifetime across drusen-containing eyes was longer than in age-matched healthy eyes. Fluorescence was observed in only the extracts from pigmented *Abca4*$^{-/-}$ mouse.

Conclusions. NIR-AOFLIO was repeatable and allowed visualization of the RPE cellular mosaic. An observed signal in only the pigmented mouse extract infers the fluorescence signal originates predominantly from melanin. Variations observed across the retina with intermediate age-related macular degeneration suggest NIR-AOFLIO may act as a functional measure of a biomarker for in vivo monitoring of early alterations in retinal health.

Keywords: fluorescence lifetime, adaptive optics, retinal pigment epithelium, infrared autofluorescence

The retinal pigment epithelium (RPE) plays an important role in maintaining the visual cycle and retinal health.[1] It constitutes a single layer of cells behind the light-sensitive photoreceptors and carries out multiple functions, including absorption of scattered light by melanin, phagocytosis of photoreceptor outer segments, waste product transport, and retinoid conversion.[2] The health of the RPE is crucial for photoreceptor survival, and its dysfunction can lead to degenerative retinal diseases such as age-related macular degeneration (AMD). For this reason, the ability to monitor and detect RPE changes is of high clinical significance. Fundus autofluorescence is one such tool that takes advantage of the naturally occurring fluorophores within the RPE to visualize morphological changes that occur late in disease, primarily originating from bisretinoid lipofuscin, melanin, and melanolipofuscin.[3–7] If the relative concentrations and composition of fluorescent molecules within each cell were to change with age and disease, then

these fluorophores could provide a prognostic biomarker to monitor RPE degeneration. Beyond fluorescence intensity, fluorescence lifetime (related to the time delay from fluorophore excitation to photon emission) has the potential to monitor cell health by characterizing differences related to variations in the fluorophore composition of the RPE. Each fluorophore has a characteristic lifetime. In the presence of multiple fluorophores, the overall fluorescence lifetime reflects their relative contributions. An advantage of lifetime measurement is that it is independent of intensity variations if enough photons are acquired to meet the threshold, and lifetime is influenced by the fluorophore environment.

Clinical fluorescence lifetime imaging ophthalmoscopy (FLIO) has identified changes between healthy eyes and those with disease using short-wavelength excitation at 473 nm.[8–12] Clinical FLIO can capture the lifetime variations with AMD[10,13] and drusen[14,15] and the changes that occur with age.[16] The fluorescence lifetime measured by clinical FLIO does not have a fine enough axial resolution to separate individual retinal layers and is confounded by fluorescence emitted from the crystalline lens.[17–19] Measuring lifetimes on the cellular scale can better isolate retinal layers and may diagnose earlier changes in disease than clinical FLIO. We have shown previously that combining adaptive optics (AO) with FLIO using short-wavelength autofluorescence (SWAF) excitation enabled imaging of the fluorescence lifetime of individual RPE cells in vivo in human subjects where the primary fluorophore was lipofuscin.[20] The use of short-wavelength light for in vivo AO imaging of human subjects is suboptimal due to patient comfort. Many patients with retinal disease have significant photophobia, and a few patient populations have greater potential for light-induced retinal damage,[21] limiting the utility of SWAF. Near-infrared autofluorescence (NIRAF) that originates from melanin has been used as an alternative to SWAF to image the RPE.[6,22,23] The use of near-infrared (NIR) light is more comfortable for the eye[24,25] and has a higher maximum permissible exposure compared to short-wavelength light. Furthermore, consistent cellular-resolved RPE images at foveal and parafoveal locations have been acquired with NIRAF imaging in an adaptive optics scanning light ophthalmoscope (AOSLO).[23,26,27] Whereas with SWAF, it is more difficult to resolve cellular structure within the fovea[23] due to lower concentration of lipofuscin within foveal RPE cells compared to peripheral RPE cells,[28,29] resulting in lower signal to noise.[3,4] In addition, absorption due to macular pigment can reduce the SWAF signal; however, this did not affect our previous AO-SWAF imaging study due to minimal absorption at 532 nm excitation light.[30,31] This motivated us to investigate NIRAF as an alternative approach to SWAF-AOFLIO. We expected that NIRAF would confer potentially more consistent RPE cellular visibility at all locations and a different molecular source of autofluorescence, which might provide insight into complementary functional biomarkers with SWAF.

Here, we demonstrate the first near-infrared adaptive optics fluorescence lifetime imaging ophthalmoscopy (NIR-AOFLIO) measurements of the in vivo human RPE mosaic. Comparison across eccentricity was performed. We also examined the variation of lifetime in two eyes with retinal abnormalities to verify the feasibility and potential of NIR-AOFLIO imaging.

Methods

NIR-AOFLIO System

A custom AOFLIO, designed previously for SWAF lifetime collection,[20] was modified to perform at NIR excitation wavelength. This was accomplished by changing the source and detector channels (Fig. 1).

A 50-ps full width at half maximum (FWHM) pulse width and 80-MHz repetition rate, supercontinuum source (SuperK EXTREME FIU-15; NKT Photonics, Birkerod, Denmark) filtered to 765/30 nm (SuperK VARIA; NKT Photonics) was used to excite the RPE cell layer. The reflected light from the eye was used to capture the NIR reflectance images in a H7422-50 (Hamamatsu Corporation, Bridgewater, NJ, USA) photomultiplier tube (PMT). Reflectance was used for location selection and coregistration with the fluorescence channel so as to reduce the overall light exposure. The employment of NIR reflectance also avoids the effects of transverse chromatic aberration caused if multiple imaging wavelengths were used. An average power of 250 to 300 µW of the NIR light at the cornea was used with an 8-mm entrance pupil at the eye. A cleanup filter (ET775/46) was used at the

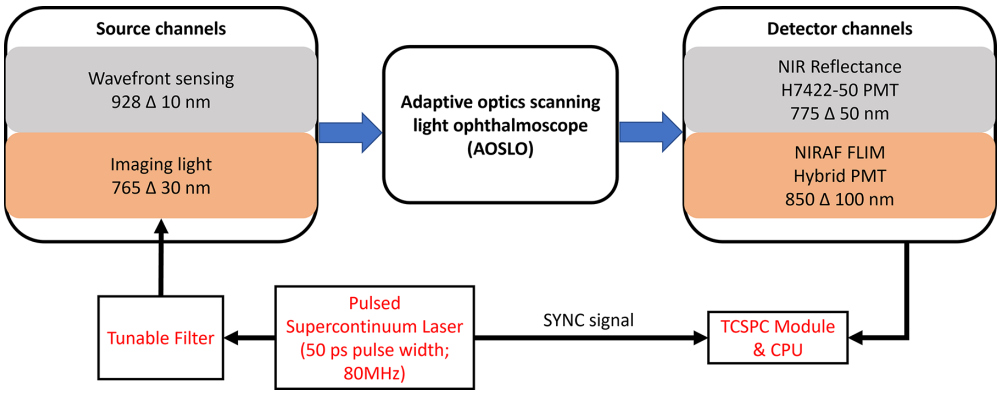

Figure 1. Modified custom-built AOFLIO. A supercontinuum laser source filtered to 765/30 nm was used for navigation and imaging of the RPE cell layer. A 928/10-nm laser diode was used for wavefront sensing and adaptive optics correction. NIR reflectance images were captured using a PMT and 775/50-nm filter. The NIRAF emission was collected from 800 to 900 nm using a hybrid PMT.

Table 1. Subject Demographics

Subject Code	Eye	Age, y	Sex	Axial Length, mm
Y1	OS	23	F	24.91
Y2	OS	23	M	25.38
Y3	OD	25	F	24.82
Y4	OD	28	F	24.07
Y5	OS	30	M	23.92
Y6	OD	35	F	25.07
Y7	OS	35	M	24.48
O1	OD	49	M	23.76
O2	OD	54	F	23.66
D1	OD	54	F	Not available
D2	OD	64	F	23.22
	OS			23.21

fiber tip to ensure that no excitation light leaked into the fluorescence channel.

In the detector channels, a long-pass dichroic (T800lpxr-xt-UF2; Chroma Technology Corp., Bellows Falls, VT, USA) was used to separate the NIR reflectance from the fluorescence signal. The reflectance images were captured through an ET775/50-nm bandpass filter (Chroma Technology Corp.) with a 1.0 Airy disk diameter (ADD) pinhole. The fluorescence signal was captured through four bandpass filters (two of ET853/93 and two of CT850/100; Chroma Technology Corp.) to exclude any stray excitation signal from the NIR source. The NIRAF light was captured using a hybrid PMT (HPM-100-50C, TE cooled; Becker & Hickl, Berlin, DE, USA) that was optimized for NIR light. To increase the signal collection, a 2.7 ADD pinhole was used for the fluorescence channel to obtain enough signal to noise. No additional longitudinal chromatic aberration (LCA) compensation was needed between the two detection channels as the wavelengths of excitation and collection were close enough and the LCA variation of the human eye across NIR wavelengths was negligible.[23] The main challenge of NIRAF imaging is the 60 times lower signal compared to SWAF,[5] resulting in the requirement of longer exposures to achieve good signal to noise.[27]

The wavefront sensing light was shifted from 850 nm (in the previous system)[20] to 928 nm (InPhenix Inc., Livermore, CA, USA) to accommodate the fluorescence collection up to 900 nm. A 900-nm long-pass cleanup filter was added at the fiber output to limit the light leakage into the fluorescence channel. An average power of 20 µW and a 7.5-mm entrance pupil size was used for wavefront sensing.

The radiant flux incident on the cornea during imaging was below the ANSI Z136.1-2014 standard considering the combined effects for both sources (765 nm and 928 nm) across the imaging field of view of 1.4° × 1.4°. A global safety shutter was in the system to block the light in case of scanner failure. The image acquisition software kept track of the total exposure time at each location to not exceed the ANSI standard.

Participants and Imaging Protocol

Seven healthy young subjects (23–35 years old, subject code Y1–Y7; Table 1) and two healthy older subjects (49 and 54 years old; subject code O1, O2; Table 1) without known ocular disease or systemic disease with ocular manifestations were imaged for this study. Additionally, two older subjects, one with intermediate AMD (54 years old; subject code D1) and one with a hyperreflective spot in the outer retina (subject code D2) in the left eye (64 years old) were imaged. Informed written consent was obtained from subjects before imaging, and all procedures were conducted according to the tenets of the Declaration of Helsinki and approved according to the University of Rochester Research Review Board.

Prior to NIR-AOFLIO, each subject underwent clinical imaging on the Heidelberg Spectralis HRA (Heidelberg Engineering, Heidelberg, Germany) to capture a 30° IR reflectance and IR fluorescence image to identify the locations of interest in subjects with pathology and help navigate the retinal space in the small field AOFLIO system. IOL Master 5 (Zeiss, Jena, Germany) was used to obtain the axial length of each eye to convert the radial units (degrees) across the retina into metric units (millimeters) in all but one subject. Mydriasis and cycloplegia were induced by administering 1% tropicamide and 2.5% phenylephrine. AMD severity grading was based on drusen size/area[32] of the imaged eye using NIR reflectance and fundus autofluorescence images.

For NIR-AOFLIO imaging, the subjects' eye was first matched with the exit pupil of the system using the live NIR reflectance image and the sharpness of the wavefront sensing spots. The location of interest was targeted by placing the subject's fixation at a specific location with a fixation target (red laser spot) through a beam splitter.[33] The vergence of the NIR imaging light on the retina was adjusted using the deformable mirror to obtain the sharpest cone reflectance image.[23] We assumed the similar vergence for NIRAF excitation due to the elongated axial point spread function in the system. It was observed by Granger et al.[23] that the sharpness of cells in NIRAF is best at the same focal plane of excitation as the photoreceptors. In this study, the imaging paradigm started with automatic pinhole optimization of the fluorescent channel at a desired location.[34] A 120-second recording simultaneously captured both the NIR reflectance of the photoreceptors and the NIR fluorescence of the RPE. Next, the beam was focused to a deeper layer (0.1 D toward RPE) using the deformable mirror, and another 120-second recording was captured to determine if the RPE cell visibility improves by going deeper into the retina from the best cone photoreceptors focus, which did sometimes improve image quality in our previous study with the short-wavelength light.[20] Also, we wanted to test the hypothesis that there would be a decrease/increase in NIRAF with a photic effect shown recently in a study on mouse retina and human donor eyes.[35] The pinhole optimization was repeated for the second focus if the subject came out of the system and reentered.

The two-image sequence was captured at seven locations in healthy subjects. The locations chosen were the fovea, 2° temporal (2T), 8° temporal (8T), 12° temporal (12T), 2° inferior (2I), 8° inferior (8I), and 12° inferior (12I). In subject D1, locations were chosen based on the location of drusen along with the fovea and 8T. Subject D2 was imaged in both eyes to compare between eyes with the chosen locations of the fovea, 8T, and region of drusen (~2T).

Data Analysis

Custom software was developed for desinusoiding and registering of fluorescence lifetime data.[36] To summarize, each fluorescence lifetime data set was coregistered using the motion trace of the simultaneously acquired IR reflectance

videos that have a better signal to noise for motion corrections and blink removals. Through this process, we were able to compensate for the eye motion, remove blinks, desinusoid the data, and combine the forward and backward scans to obtain strip registered histogram lifetime data at each pixel. The histograms' output from the custom software was then uploaded to the commercial SPCImage software (Becker & Hickl, Berlin, Germany). A maximum likelihood estimation algorithm was used at each pixel to generate a two-component exponential decay curve fit ($a_1e^{-t/\tau_1} + a_2e^{-t/\tau_2}$) with the individual lifetime components (τ) and their relative contributions (a). The weighted mean lifetime at each pixel was calculated by $(a_1\tau_1 + a_2\tau_2)/(a_1 + a_2)$. A threshold of 300 photons within each kernel was used as a limit to reduce the background noise.[37] An instrument response function (IRF) was measured in the system and deconvolved during the decay curve fitting for an accurate fit of the lifetime components.[38] For all young human subjects' data, a kernel of 15 × 15 pixels was used that corresponds to about 11.13 µm in the retina. For older subjects (49–64 years old) and subjects with retinal abnormalities, a higher kernel of 21 × 21 pixels was used due to lower signal intensity. Mean and standard deviation across each image were computed. To compare any lifetime data, we had to be at the same kernel size due to the variations in lifetime that occur from SPCImage software by changing the kernel (refer to Supplementary Fig. S1). The kernel used in the study does not reduce the number of pixels in each image but rather combines data from surrounding pixels for the lifetime data used with exponential fitting (referred to as binning by Becker & Hickl).[38]

Phasor analysis was also performed for each image along with the histogram data. Phasor plot provides a way to view relative contributions of fluorophores within a living tissue.[39] At each pixel, the registered decay curves and the exported measured IRF from SPCImage were used to calculate the discrete Fourier transform evaluated at the pulse repetition frequency of the excitation source using a custom MATLAB script. The real (g) and imaginary (s) components at each pixel resulted in the two-dimensional phasor plot (g,s).[40,41] The mean and standard deviations of g and s for each image were calculated for further analysis. Repeatability between the two visits in four subjects was assessed by intraclass correlation (ICC). Significance is deemed for $P < 0.05$.

Retinal Fluorophores and Mouse Extracts

There are many endogenous fluorophores in the retina. Although they might not be excited with NIRAF, we explored if a number of potential retinal fluorophores contributed to the fluorescence signal. We also imaged extracts from agouti (brown) and albino *Abca4*$^{-/-}$ mice.

Nicotinamide adenine dinucleotide (NADH) (Sigma, St. Louis, MO, USA; N8129) present in all cells and retinal layers with excitation and emission maximum (Ex_{max}, Em_{max}) of (375 nm, 475 nm) was prepared in Tris HCl. Flavin adenine dinucleotide (FAD) (Sigma; F6625) present in all cells and retinal layers with Ex_{max} = 410 nm and Em_{max} = 540 nm was prepared in milliO water and PBS.[42] The retinoids common to the photoreceptor and RPE layers, all-trans-retinol (ROL) (Sigma; R7632) with absorbance maximum at 320 nm and all-trans-retinal (RAL) (Sigma; R2500) with absorbance maximum at 380 nm,[43] were prepared in ethanol. Elastin (Sigma; E1625), a structural molecule with (Ex_{max}, Em_{max}) of (315 nm, 405 nm),[44] was prepared in Tris HCl. Carotenoids lutein (Ex_{max} = 445 nm) (Kemin Health, Des Moines, IA, USA) and zeaxanthin (Ex_{max} = 451 nm)[45] (Kemin Health) were prepared in ethanol.

Each sample was imaged at the retinal conjugate plane in UV-polymer cuvettes (Mfr. No. 759200; BrandTech Scientific, Essex, CT, USA) (Huynh KT. IOVS 2022;63:E-Abstract 394–F0432).[46] The solutions were heated to 37°C in a water bath and imaged using NIR-AOFLIO. Additionally, light-sensitive fluorophores were prepared under red light conditions. The collected signal was considered a null result if the photon count was below the system collection threshold (signal-to-noise ratio below an inflection point in our system to measure signal that is higher than the background and back-reflections from an empty cuvette).

Samples from *Abca4*$^{-/-}$ agouti (brown) mice eyes, which were obtained by extraction of retinas with chloroform and methanol, were also imaged.[47,48] These extracts would contain many fluorophores from the entire retina, including bisretinoids, vitamin A, and possibly FAD and NADH. The *Abca4*$^{-/-}$ mouse model accumulates elevated levels of bisretinoid lipofuscin in the retina and is a model of recessive Stargardt disease.[49] One eye each of both pigmented and albino extracts was used to compare the change in lifetime with the presence or absence of melanin, respectively. The extracts were dissolved in methanol solution, and the lifetime was measured at 37°C in a cuvette using NIR-AOFLIO.

Results

Registered and desinusoided NIRAF images revealed the hyper-AF borders and hypo-AF centers of the RPE cells at all seven eccentricities (Figs. 2b_1–b_7). The maximum fluorescence intensity signal was observed at the fovea and decreased with eccentricity. Within the cohort of young subjects, cellular structure was observed at all seven eccentricities in five subjects and in three locations in two. One of the two subjects in whom cells were not seen in all locations had large eye motion artifacts, resulting in removal of multiple frames after registration, although the photon counts were comparable across the young subject cohort. In a comparison of two NIRAF intensity images captured at each location with 0.1 D defocus difference, no change in RPE cell visibility was observed with most of the images acquired.

Repeatability of NIR-AOFLIO Across Multiple Visits and Exposures

The current study shows the feasibility of AO NIRAF in all subjects imaged. To study the repeatability of NIR-AOFLIO in our study, four of seven younger normal subjects were imaged across two visits 1 to 8 weeks apart. To compare the lifetime across multiple visits at the same locations, registered NIR reflectance images were used to find the overlapping regions in both visits. A mask was applied on the mean lifetime data to select the common pixels across both visits. An example data set is shown in Figure 3, where NIR reflectance (Figs. 3A, 3D) and NIRAF intensity (Figs. 3B, 3E) images from both visits were cropped to obtain the common overlapped region and the mean lifetime plots

Investigative Ophthalmology & Visual Science

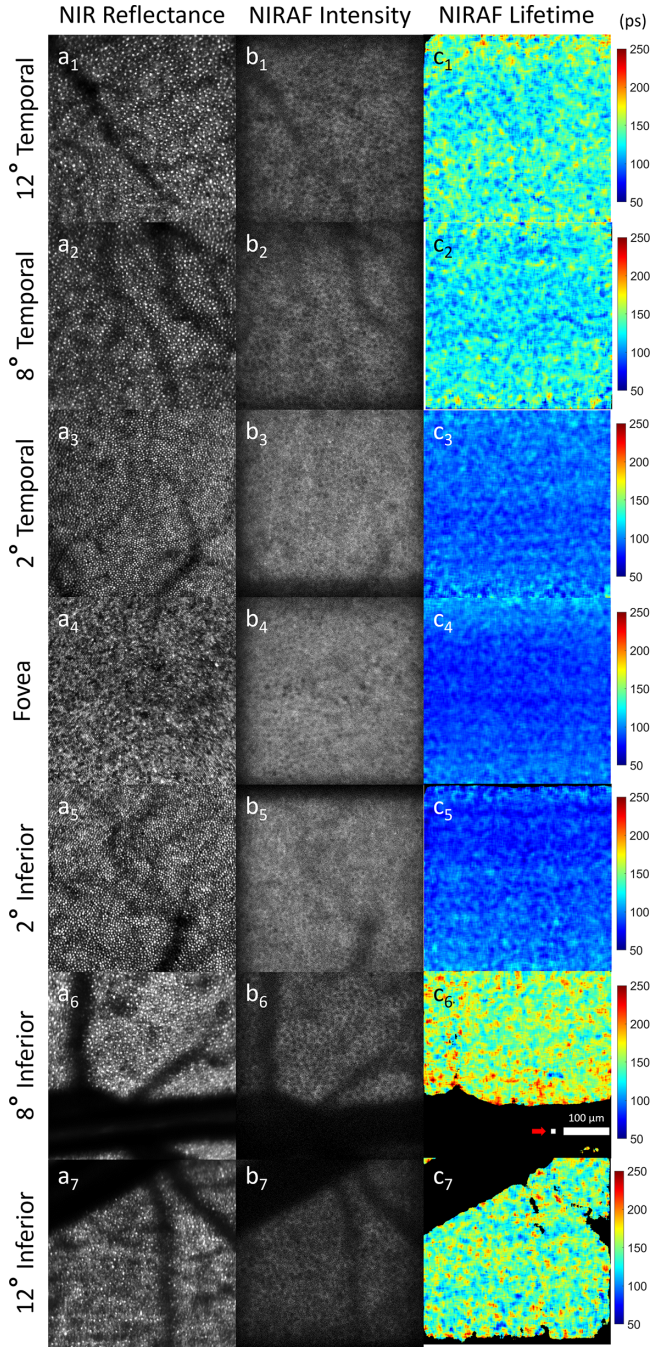

Figure 2. NIR-AOFLIO images in a young healthy subject (Y4) at seven eccentricities. (**a_1–a_7**) NIR reflectance cone mosaic. (**b_1–b_7**) Coregistered NIR fluorescence images revealing the hyper-AF borders and hypo-AF centers at all locations. (**c_1–c_7**) The registered lifetime images at each location. Kernel size in pixels (*white box* and *red arrow*) and *scale bar* (*white bar*) are shown in **c_6**.

(Figs. 3C, 3F). Histograms of mean lifetime and the phasor distribution across both visits showed good repeatability (Figs. 3G, 3H). Figure 4 shows the correlation between visit 1 and visit 2 for each lifetime component across the four subjects. All parameters were repeatable between two visits, with an ICC of 0.87 (τ_m), 0.75 (τ_1), 0.66 (τ_2) 0.98 (a_1), 0.90 (g), and 0.92 (s).

An intrasubject multivariate analysis was performed on exposure 1 and exposure 2 mean lifetime data at each eccentricity for all young subject data sets to determine if significant changes occurred with multiexposure photic effect due to NIR light exposure.[35] Interestingly, a significant difference in mean lifetime was observed between exposures 1 and 2 at each retinal location during both visits (τ_m: $P = 0.031$). For 93% of the data sets analyzed with exposure 1 and exposure 2, the lifetime increased or was similar. However, when intrasubject variability of both exposures was compared across both visits, the result tended toward a significant difference ($P = 0.056$), although the intersubject variability of mean lifetime with exposure and visit as factors at each eccentricity showed no significant difference ($P = 0.461$). In summary, high repeatability of mean lifetime was observed only when each exposure data (either exposure 1 or exposure 2) were compared separately across both visits. To remove dependency of change in lifetime with exposure, we analyzed and compared data only from the first exposure in the rest of the article. This is not the same as the long-term reduction in NIRAF signal that was observed by Masella et al.[50] in nonhuman primates.

NIR-AOFLIO With Eccentricity

The fluorescence intensity and the lifetime data were coregistered with the IR reflectance to obtain a desinusoided registered lifetime image (Figs. 2c_1–c_7). Among the 150 data sets (images) collected from seven young normal subjects, about 10% of the collected images resulted in failed registration due to large involuntary eye motion. From the remaining images, successful exponential lifetime fits were generated for about 90% of the images while the remaining 10% of the images did not generate any exponential fit due to lower than minimum required photon count. Additionally, any image with less than one-third of the pixels above threshold was excluded. A substantive variation in lifetime was observed across eccentricities, where the lifetimes at the fovea locations (0° and 2°) (Figs. 2c_3–c_5) were shorter compared to near-peripheral locations (8° and 12°) (Figs. 2c_1, 2c_2, 2c_6, and 2c_7). Comparing the histograms of mean lifetime for each of these eccentricities in subject Y4 (Fig. 5A), the foveal locations trended with lifetimes below 100 ps and the near-peripheral locations with lifetimes above 100 ps, forming a clear separation. There was an average difference of mean lifetime of 38.6 ps between the fovea to near-peripheral regions. The phasor plot in subject Y4 (Fig. 5B) showed a similar effect with the near-peripheral clusters separated from the foveal clusters.

For all seven young healthy eyes, the lifetime components τ_m, τ_1, τ_2, and a_1 were plotted versus eccentricity in Figure 6. A trend toward a change in all exponential decay curve components as a function of eccentricity was observed in all subjects. The τ_m, τ_1, and τ_2 were longer with larger eccentricities, and a_1 decreased with larger eccentricities. Table 2 shows the mean of each lifetime component across all younger normal eyes at each eccentricity. Figure 7 shows mean and standard deviation across all healthy young subjects of the g and s components of the phasor data for all eccentricities imaged. The zoomed insert in the phasor plot shows a similar difference observed as a function of eccentricity where the foveal regions and near-peripheral regions formed separate clusters.

Investigative Ophthalmology & Visual Science

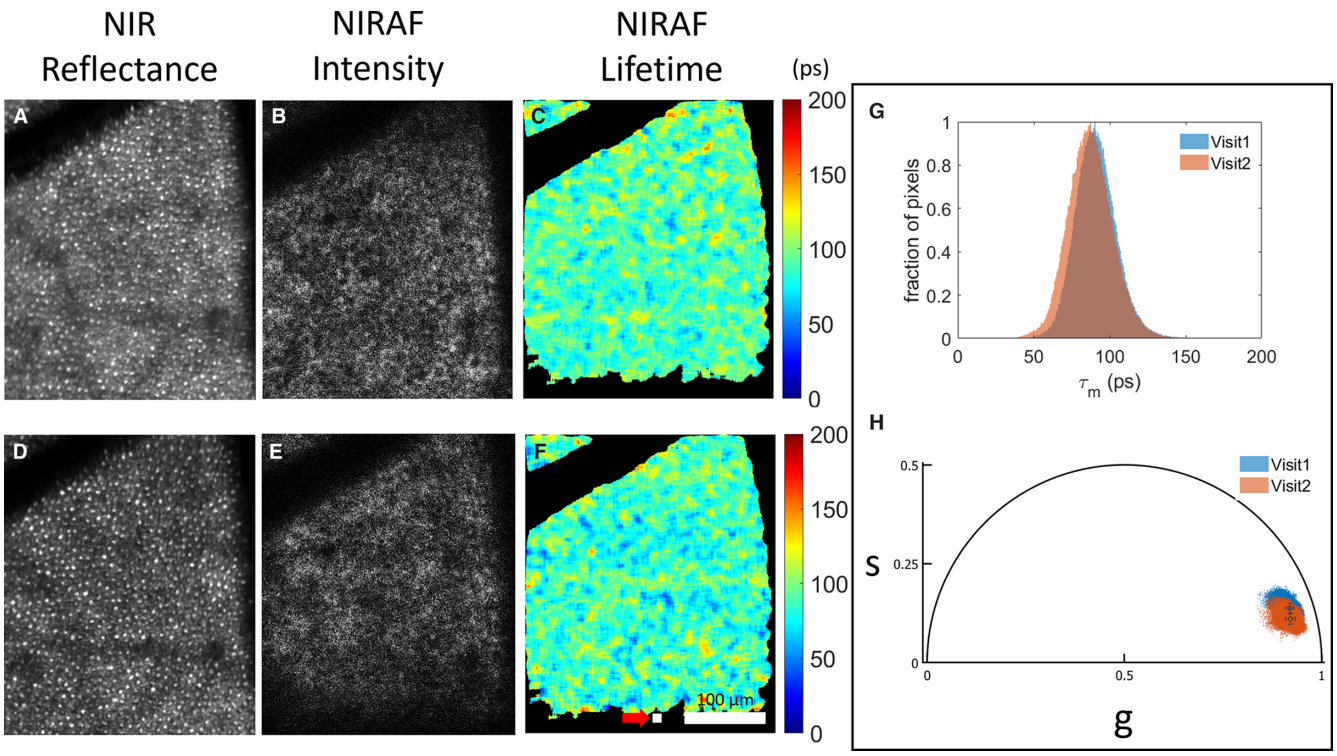

Figure 3. Repeated imaging across two visits in subject Y5 at 8° inferior. (**A**, **D**) Registered NIR reflectance images for visit 1 and visit 2, respectively. (**B**, **E**) The NIRAF intensity. (**C**, **F**) The NIRAF mean lifetime images. (**G**) Histogram and (**H**) phasor data comparison across two visits showing good repeatability. Kernel size in pixels (*white box* and *red arrow*) and *scale bar* (*white bar*) are shown in **F**.

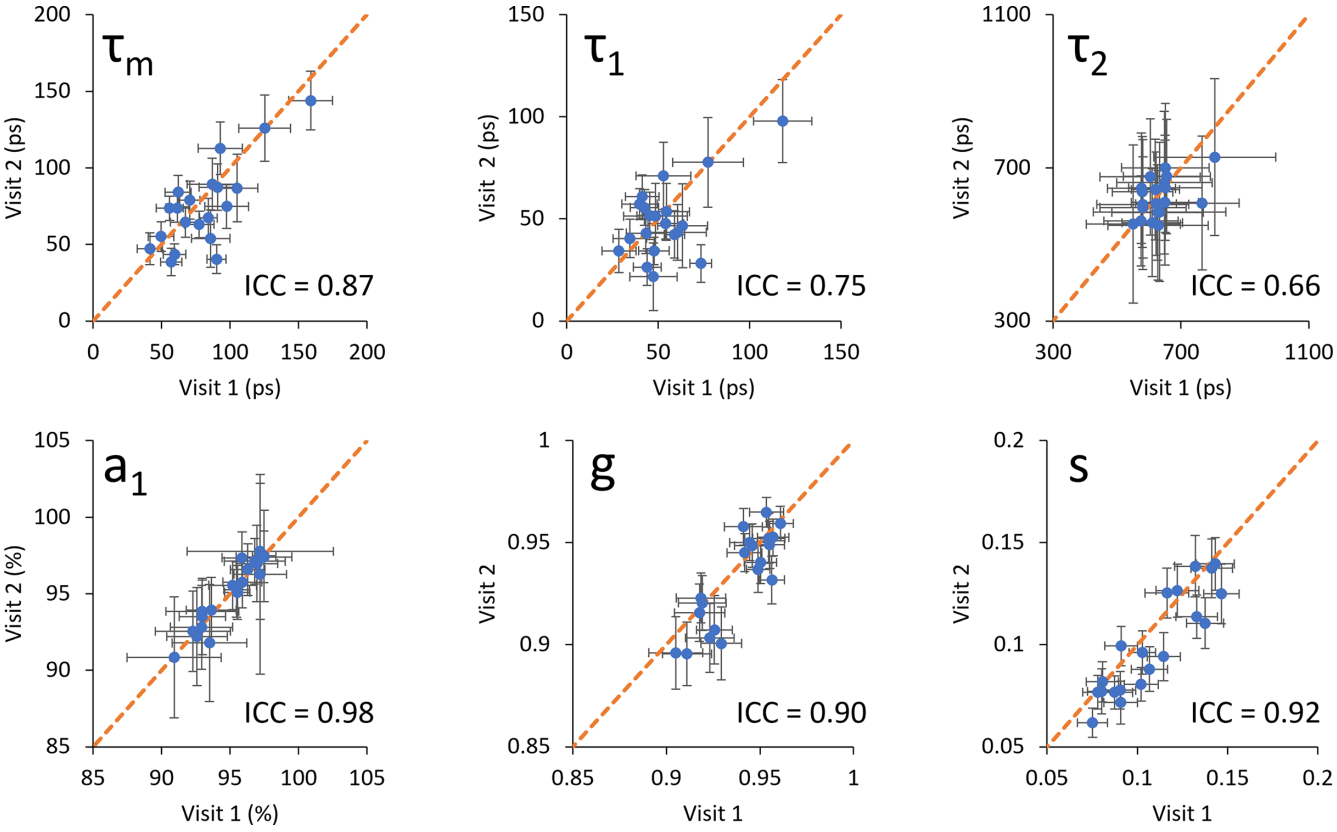

Figure 4. Visit 1 versus visit 2 plots for the lifetime coordinates τ_m, τ_1, τ_2, and a_1 and the phasor coordinates g and s. Each data point represents the average value of the coordinate across each image plotted against two visits along with the standard deviation across the image. ICC values show moderate to excellent correlation between visits. The *orange dashed line* in each plot represents the line for perfect correlation.

Investigative Ophthalmology & Visual Science

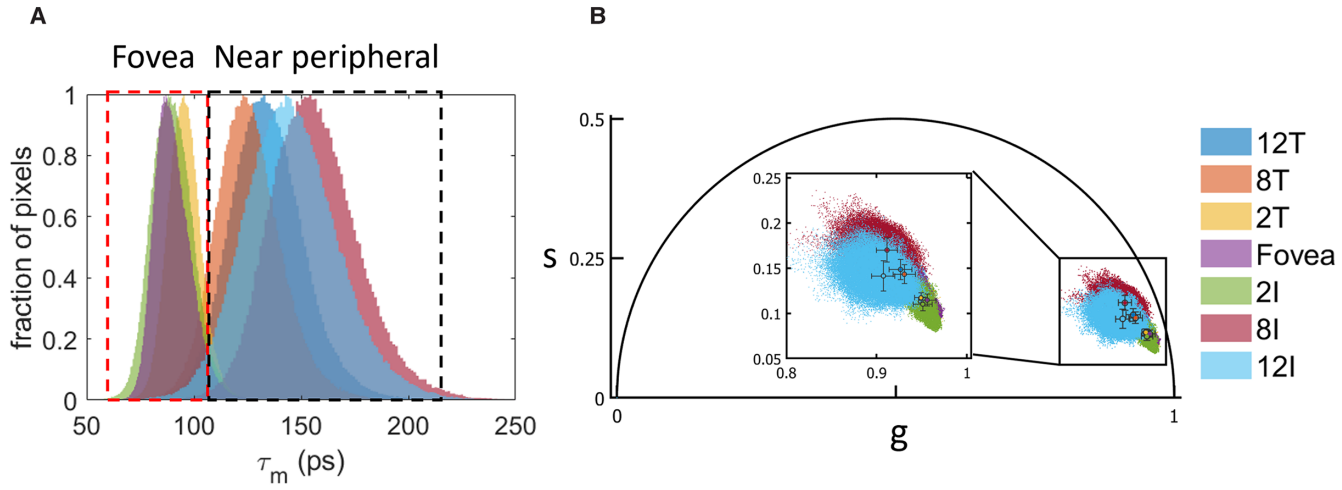

Figure 5. (**A**) Normalized histograms at each eccentricity for subject Y4 (from locations in Fig. 2) and the lifetime difference between the fovea and near-peripheral locations. (**B**) The phasor plot for the locations showing a similar trend as the lifetime.

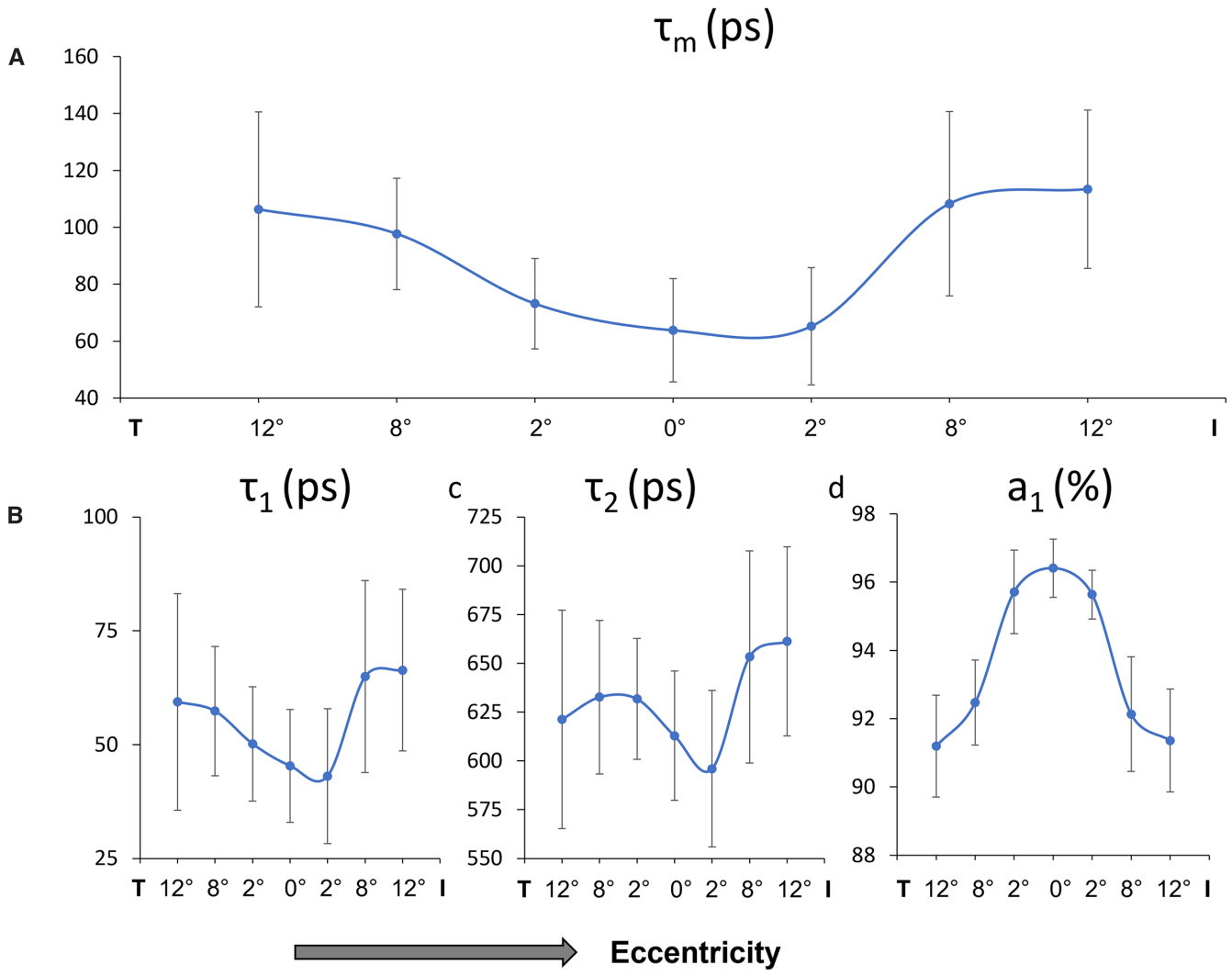

Figure 6. (**A**) Combined τ_m data plot of all healthy younger normal subjects showing the variation across the seven eccentricities imaged. Similar variations in individual lifetime components are shown for (**B**) τ_1, (**C**) τ_2, and (**D**) a_1 (%), respectively.

Table 2. Mean (M) and Standard Deviation (SD) of Lifetime Components for All Healthy Young Normal Subjects at Seven Eccentricities

	τ_{mean}(ps)		τ_1(ps)		τ_2(ps)		a_1(%)	
Imaging Location	**M**	**SD**	**M**	**SD**	**M**	**SD**	**M**	**SD**
12° Temporal	106.3	34.3	59.4	23.8	621.3	56.0	91.2	1.5
8° Temporal	97.7	19.6	57.4	14.2	632.7	39.3	92.5	1.2
2° Temporal	74.4	17.1	50.6	13.0	633.3	30.8	95.6	1.3
Fovea	63.8	18.1	45.3	12.4	612.8	33.1	96.4	0.9
2° Inferior	65.2	20.6	43.1	14.8	596.0	40.1	95.6	0.7
8° Inferior	108.3	32.4	64.9	21.1	653.3	54.4	92.1	1.7
12° Inferior	113.4	27.8	66.4	17.8	661.3	48.5	91.4	1.5

Lifetime Measurements of Retinal Fluorophores and Mouse Extracts

All the solutions of endogenous fluorophores (NADH, FAD, elastin, ROL, RAL, lutein, and zeaxanthin) imaged in the cuvettes gave a null result for the NIRAF collection. For the extract solutions, the total photons collected in the albino extract were very low compared to the pigmented extract (albino/pigmented = 1:25) for the same acquisition time, and the signal in the albino extract was close to the noise floor of the detector and was not deemed to be a good signal for comparison. The mean lifetime of the pigmented mouse extract was 449.2 ± 10.2 ps. The phasor data from pigmented mouse extract are shown in comparison to the average phasor data from all younger normal human subjects (Fig. 7).

NIR-AOFLIO Analysis of Eyes With Retinal Abnormalities

Subject D1, exhibiting intermediate AMD, was imaged with NIR-AOFLIO (Figs. 8C, 8D). IR reflectance from clinical confocal scanning laser ophthalmoscope (cSLO) showed the regions of interest (ROI; Fig. 8A). Each area imaged with NIR-AOFLIO was color coded with the ROI in the cSLO IR reflectance image as a visual aid. Along with the fovea and 8° temporal sites, four locations within 2° to 3° temporal (blue dots for visual aid) were imaged for comparison with three healthy age-matched (49–64 years old) older eyes at similar eccentricities. Figures 8C and 8D show the variations in lifetimes and intensity at each location and eccentricity imaged in subject D1. Figure 8E presents comparisons of the average lifetime data at each eccentricity for the three healthy eyes relative to the AMD eye. The mean lifetimes at the four locations in subject D1 were captured at 2° to 3° eccentricity and averaged. At 2° to 3° eccentricity, the mean lifetime was longer in subject D1 compared to age-matched older healthy eyes at 2° eccentricity ($\tau_m = 97.9 \pm 18.0$ ps vs. 67.1 ± 38.2 ps). The 8° temporal location also had a longer mean lifetime for subject D1 compared to the average data of the three healthy eyes ($\tau_m = 126.2 \pm 25.5$ ps vs. 78.6 ± 24.8 ps). The foveal data acquired from subject D1 do not appear to be different compared to older healthy eyes (Fig. 8E). Figure 8F shows the plot of means and standard deviations of phasor data along with the zoomed insert. The mean and standard deviation of phasor data at 2° temporal show a trend similar to the mean lifetime, with the AMD eye exhibiting a longer lifetime. For the phasor data, differences between subject D1 compared to the control data were more difficult to interpret than the mean lifetime.

Subject D2 was also imaged with NIR-AOFLIO. Clinical cSLO IR reflectance images from left (Fig. 9A) and right (Fig. 9B) eyes were captured prior to AO imaging. The left eye exhibited a hyperreflective focus (Fig. 9A). The fluorescence lifetime of the fovea and 8° temporal regions was captured in addition to the hyperreflective spot and compared to the fovea and 2° and 8° temporal regions in the clinically normal right eye. The Optical coherence tomography (OCT) B-scan from the left eye is also shown (Fig. 9C). AO NIR reflectance images revealed intact cone mosaic outside the hyperreflective lesion (Fig. 9D), and RPE cells could be observed in the AO NIRAF montage in the surrounding hyperreflective spot (Fig. 9E). Figure 9G shows the comparison of mean lifetime in the eye with the lesion relative to similar eccentricities in the clinically normal eye.

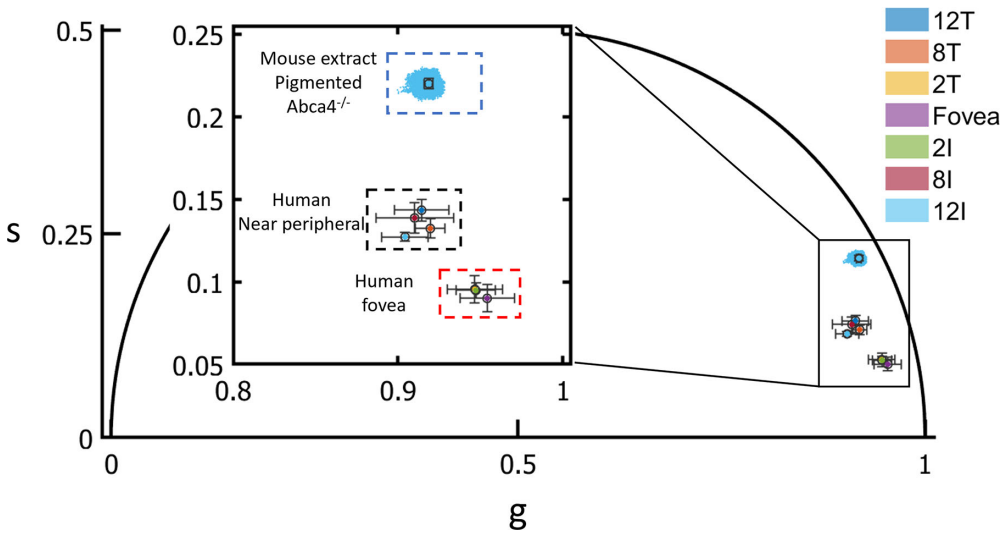

Figure 7. Combined phasor data for all healthy younger subjects acquired at seven eccentricities revealing the difference between the fovea (*red box*) and near-peripheral regions (*black box*). Also shown are the phasor data acquired from a pigmented *Abca4*$^{-/-}$ mouse extract (*blue box*) using NIR-AOFLIO.

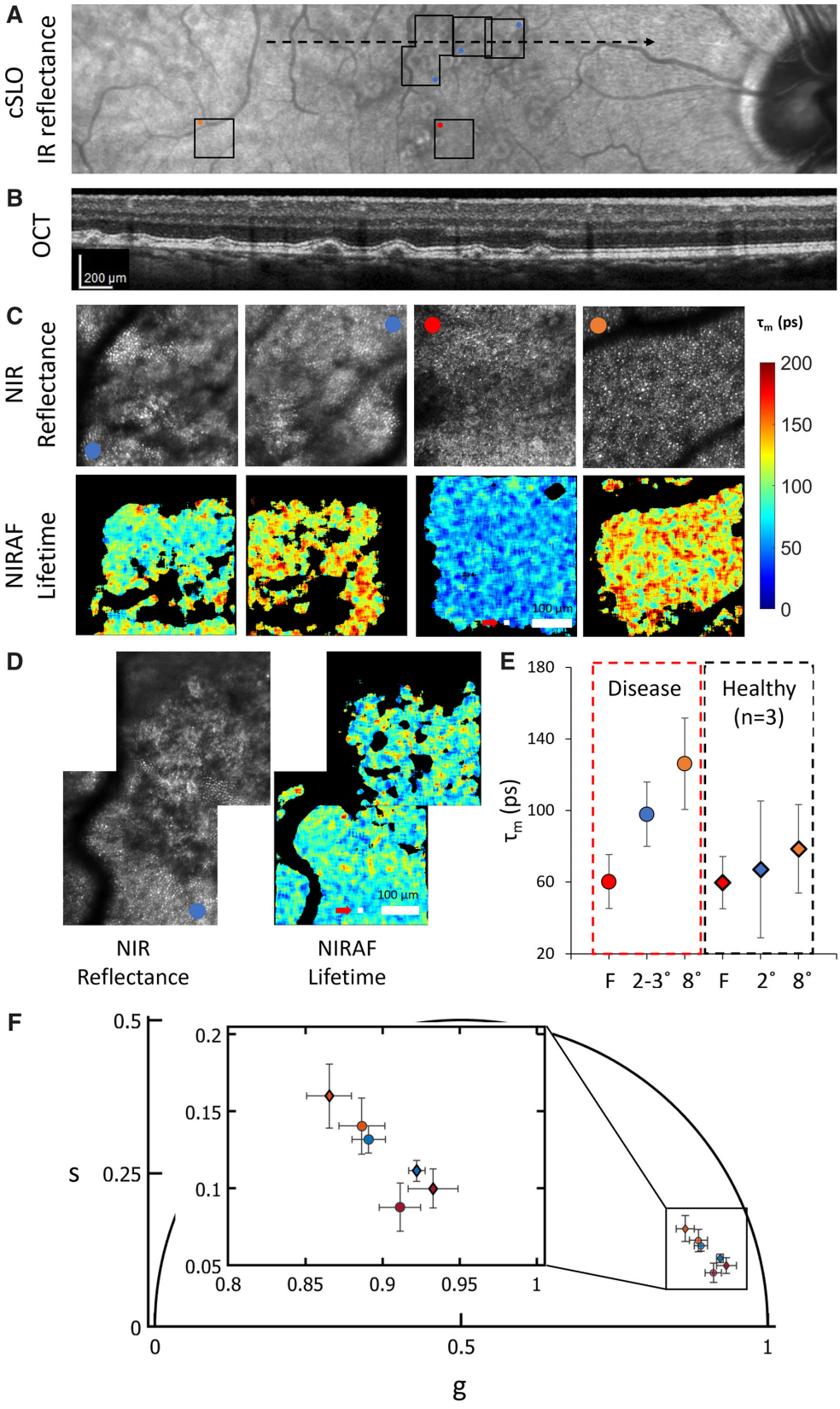

Figure 8. Clinical cSLO IR reflectance (**A**) in subject D1 shows multiple ROIs imaged by AO. (**B**) Optical coherence tomography (OCT) B-scan showing the sub-RPE deposits in the outer retina. AO imaging shows photoreceptor NIR reflectance and lifetime of various ROIs (**C**, **D**). Comparison of lifetimes at various eccentricities in diseased and healthy eyes (**E**). The corresponding phasor data are presented (**F**). The kernel size in pixels (*white box with red arrow*) and *scale bar* (*white bar*) are shown in **C** and **D**.

Investigative Ophthalmology & Visual Science

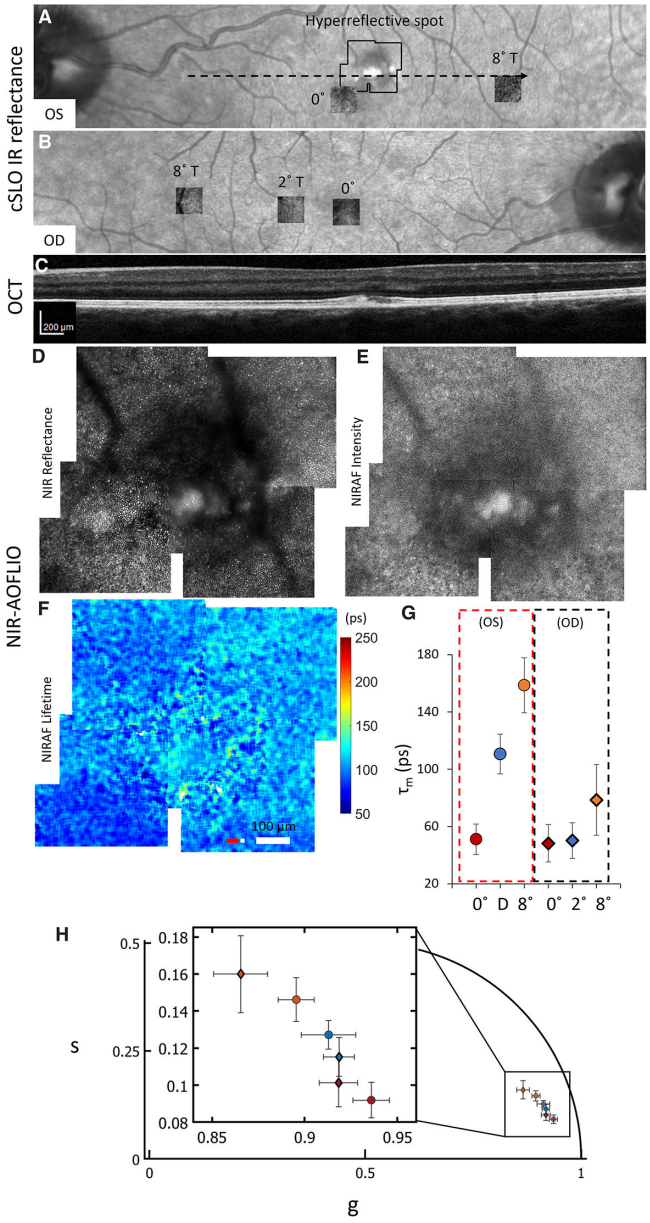

Figure 9. Clinical cSLO IR reflectance (**A**) in left eye of subject D2 shows a small spot of hyperreflectivity overlapped with the ROI for AO imaging. (**B**) Imaging locations in the normal right eye of the same subject. (**C**) OCT B-scan shown across the hyperreflective spot. Montage of the ROI using NIR-AOFLIO showing photoreceptor NIR reflectance (**D**), NIRAF (**E**), and the lifetime (**F**). Comparison across both eyes using mean lifetime (**G**) and phasor data (**H**). The kernel size in pixels (*white box with red arrow*) and *scale bar* (*white bar*) are shown in **F**.

Because of the small sample size, no statistical analysis was performed. The ROI that included the hyperreflective spot (~2° temporal) and 8° temporal region had longer lifetimes (τ_m = 110.6 ± 13.9 ps and τ_m = 158.6 ± 19.2 ps, respectively) compared to the healthy eye (τ_m = 50.1 ± 12.5 ps and τ_m = 78.6 ± 24.8 ps, respectively), while fovea in both eyes showed a similar lifetime. The plot of mean and standard deviation of phasor distribution (Fig. 9H) at each location in both eyes shows a similar effect with lifetime increasing as a function of eccentricity. The phasor distribution of the ROIs within the lesion-containing left eye (blue circle) tended toward longer lifetimes as compared with the eccentricity-matched healthy eye (blue diamond). But at the 8° location, the eye with a hyperreflective spot (orange circle) did not show a substantial difference when compared to the 8° location in the healthy eye (orange diamond). Future imaging studies that include more subjects and imaging locations will be required to get a confidence interval related to mean lifetime and disease progression. The change associated with the hyperreflective lesion may indicate an adjustment in the environment of the cell.

Discussion

This study demonstrates the first fluorescence lifetime data captured with NIR excitation of the in vivo human RPE cell mosaic. In vivo cell visibility in humans is a major advancement in AO imaging technology. Multiple studies have been conducted to show the feasibility of AO NIRAF across multiple subjects.[23,27,51] The method of desinusoiding and registering the lifetime data is critical for obtaining consistent cellular scale images of the RPE mosaic. The cellular mosaic visibility due to differences in fluorescence intensity reflects the contrast between the bright borders and dark interiors of each cell. This is possible because the nucleus is not autofluorescent and thus not likely to contain any relevant fluorophores, and the nucleus may also block emission from sources located inferiorly in the cell.[23,26,34,52] In the lifetime images, we do not expect to observe the RPE mosaic, as the lifetimes are independent of intensity. Since the excited fluorophore is distributed across each cell,[53,54] we expect the fluorescence lifetime to vary across the cell and in between cells. The fluorescence intensity images and the fluorescence lifetime images have an equal number of pixels. The cell visibility and lifetime fitting success rate of NIR-AOFLIO were very good for younger normal subjects. For older subjects with clinically normal eyes or with AMD, the foveal locations gave the best cell visibility as a result of a higher photon count likely due to higher optical density of melanin in the fovea.[5,29] Of the 12 near-peripheral locations imaged in older subjects, seven locations did not meet the minimum photon threshold criterion of 300 photons per pixel, even with the use of a larger kernel. The system's lateral resolution is about 2 µm FWHM with an axial spread of about 30 to 40 µm FWHM for the NIR fluorescence imaging.[55] Because of the large kernel, the lateral sampling of the lifetime data in our system was larger than the diffraction limit. For all younger normal subjects, we used a kernel size of 15 pixels, which corresponds to about 11.1 × 11.1 µm. Due to low photon count in the older subjects, we used a larger kernel size of 21 pixels, which corresponds to about 14.7 × 14.7 µm. The major limitation of NIRAF is the lower photon count compared to SWAF, which determines the kernel size and the ability to observe cellular-level changes. Longer exposures will increase photon count collection and may improve image acquisition in older adults and in people with disease. Nonetheless, we have demonstrated successful NIR-AOFLIO in vivo in healthy humans and two subjects having retinal abnormalities. To our knowledge, no clinical data or instrument has been built that captures the fluorescence lifetime of in vivo RPE at NIR excitation. Thus, no direct clinical comparison could be made.

One advantage of NIR-AOFLIO is that cell visibility is consistent at most of the locations when the photon threshold is met. Another advantage of NIR over SWAF is that NIR

light requires no additional chromatic aberration compensation between the NIR reflectance and NIRAF for coregistration for eye motion compensation. Also, the hemoglobin absorption at NIR wavelengths is lower[56] and can aid in imaging cells beneath smaller blood vessels. It can also be advantageous in imaging older aged eyes with natural lenses that have reduced transmission at short wavelengths.[57] Finally, in terms of the imaging system, use of just one source to gather both reflectance and fluorescence lifetime images is less challenging and may be better for clinical transition.

Strong evidence that the NIRAF signal measured in this study is related to melanin derives from the observation that fluorescence was emitted only by the extracts acquired from the pigmented *Abca4*$^{-/-}$ mouse model. The relationship between SWAF and NIRAF has been studied previously.[58] Consistent with the current findings, it was reported that NIRAF originates predominantly from melanin. Nevertheless, in patients carrying mutations in *ABCA4* that confer increased bisretinoid lipofuscin in RPE, the increase in SWAF (emitted from bisretinoid) was paralleled by a generalized increase in NIRAF signal.[58] Similarly, the NIRAF signal in pigmented *Abca4*$^{-/-}$ mice was more pronounced than in pigmented mice having wild-type levels of bisretinoid. Imaging of the endogenous fluorophores (NADH, FAD, ROL, RAL, elastin, lutenin, and zeaxanthin) gave a null result as expected due to the excitation wavelength of each of those outside the excitation bandwidth of the source (NIR).[42–45] Nevertheless, testing of the endogenous fluorophores ensured that in NIR-AOFLIO, no background signal was present that might have caused the observed lifetime changes due to the axial spread of the point spread function.

It was suggested that since density-dependent self-absorbance of the emission from melanin occurs,[59] quenching of the NIR fluorescence emission by secondary absorbance could be reduced if the packing density of melanosomes was altered by the interspersion of lipofuscin-containing organelles with melanosomes. In this way, a more pronounced release of the fluorescence emission of melanin could occur. On the other hand, this scenario did not account for the observation that in albino *Abca4*$^{-/-}$ mice, fundus NIRAF intensities were elevated in tandem with increases in bisretinoid lipofuscin even in the absence of melanin.[59] Since bisretinoids undergo photooxidation, the reduced signal in the albino mice could also be due to reduced levels of bisretinoid compared to the pigmented extracts.[60]

The difference in the phasor plot between the pigmented mouse extract and human data in this study may be accounted for due to measurement in ex vivo samples (in the case of mouse). While lifetime measurements of melanin have been reported in literature, most are related to skin pigment,[61–63] hair,[64] or choroidal melanin.[65–68] Due to the abundance of various types of melanin and its broad excitation (300–800 nm) and emission spectrum (broad in the NIR range),[18,69] the comparison of the lifetimes measured in this study to the lifetimes in other published work is difficult.

The longer lifetime at near-peripheral locations compared to the fovea was consistent between subjects and observed in both exponential decay fitting and the phasor plots. The optical density of melanin has been reported in human eyes to be highest at the fovea and to decrease with eccentricity.[5,29] A similar result for NIRAF has been reported where the number of photons captured at the fovea was highest with NIR excitation[23,27] pertaining to higher melanin optical density. In our study, we observed a similar effect with the collected photon counts highest at the fovea. The mean lifetime was shorter at the fovea and became longer with eccentricity. The sources of NIRAF signal have been reported to be dependent on melanin optical density, in some cases lipofuscin, and the effect of fluorescence quenching by secondary absorbance due to packing density. The variation in the relative contribution (a_1) of the shorter lifetime component (τ_1) is possibly due to changes in optical density or the amount of melanin as a function of eccentricity. This, in turn, could account for the increased variation of mean lifetime. On the other hand, the variation of melanosome distribution as a function of eccentricity could lead to changes in the amount of quenching of NIRAF and microvariations in the local environment that affect lifetimes.[70,71] This could also explain small variations in the short and long lifetimes (τ_1, τ_2) observed in the study. In addition, we may not have accounted for all fluorophores that are contributing to the NIRAF. A2E is one such fluorophore abundant in the parafovea compared to the fovea, which was not tested and could play a role in the variation of the lifetime.

Melanin in the retina has been reported in the literature to play a role in protecting against photic and oxidative injury.[72] It has also been shown/hypothesized that NIRAF arises from melanin degradation products and that the NIRAF signal changes with photic or oxidative stress.[35,73] However, the role of melanosomes is complex. They can both protect against and promote photooxidative reactions, depending on the microenvironment and the level of oxidant exposure.[74,75] Previous research demonstrated that infrared illumination reduces NIRAF, with partial recovery after 1 month.[50] This suggests that light exposure could alter the microenvironment and the fluorophores being imaged, potentially due to oxidized melanin. This could explain the lifetime changes observed with the exposures utilized in our study. Photooxidative processes initiated by bisretinoid[60,76] may be responsible for melanin oxidation, particularly in the case of melanolipofuscin. It should also be noted that, when comparing the two NIRAF intensity images captured at each location with 0.1 D defocus difference, no change in RPE cell visibility was observed with most of the images acquired. Future studies could measure the lifetime changes in response to prescribed light exposures with variable power and time to better understand the role of melanin oxidation and lifetime variation. The time scale for the recovery to baseline fluorescence lifetime following initial light exposure is unknown but may be on the order of hours or days. Repeated measures at multiple visits showed repeatability and consistency up to 8 weeks from the first exposure. This demonstrates the feasibility of NIR-AOFLIO as a technique to observe functional changes in RPE longitudinally with aging or disease progression.

The proof-of-concept imaging in eyes with intermediate AMD revealed lifetime variations as a function of eccentricities that were different than in healthy eyes in older subjects. In addition, the subject with an abnormal hyperreflective lesion in outer retina exhibited a longer lifetime in clinically normal regions as well (8° temporal). A recent clinical FLIO study reported a similar effect in clinically normal subjects but with few small drusen; in the fundus was a specific ring-shaped pattern with longer lifetimes similar to the pattern observed in the AMD cohort.[13] This begs the question as to whether lifetime variations can be detected before focal clinical changes occur in early AMD. More longitudinal studies are needed to validate this change. The NIRAF images

Investigative Ophthalmology & Visual Science

obtained in subject D1 did not provide structural evidence of individual RPE cells (see Supplementary Fig. S2). It is unlikely that our images did not capture the layer of interest since photoreceptor cells were clearly visible in images acquired in the NIR intensity channel, indicating that to resolve RPE cells, the plane of focus was appropriate. A more likely possibility would be that the RPE cells had assumed a multilayered cell structure often observed in later stages of AMD.[77] It is presumed that the cellular structure of RPE is observed due to the contrast between the nucleus and surrounding lipofuscin granules. If the RPE monolayer is disrupted, the contrast difference may not be observed with our imaging systems; this is similar to that reported by Rossi et al.[34] Although the cellular structures were not observed in the NIRAF images, the advantage of lifetime analysis is the ability to acquire and analyze the data, provided that the threshold of collected photons is reached. The data acquired at the 8° temporal location in subject D1 indicate differences between control and intermediate AMD in terms of mean lifetimes and phasor analysis. At first glance, this may appear contradictory. However, the translation from one space to another is not a linear effect. The lifetime exponential decay metric assumes a fixed number of contributing fluorophores (two in the case of our data sets), but the phasor approach does not make this assumption and can have many contributing fluorophores. The actual similarity between the variation would have been linear if the individual lifetime components (τ_1 and τ_2) remained the same when comparing the two data sets. But this was not the case with NIR-AOFLIO data, where τ_1 and τ_2 also changed along with the τ_m. The data are even more complicated as any given point in the phasor space can have multiple solutions. They are not direct correlates to each other. A similar effect was observed in another study in which S cones were distinguished in the phasor space while no such difference was observed in the mean lifetime space.[78] More specifically with our 8° temporal data set, the τ_1 and τ_2 values acquired from the eye with the hyperreflective spot were 94 ps and 707 ps, while that of the subject's other eye were 32 ps and 557 ps. As each of the individual data points changes in phasor space, the combined effect can sometimes be nonlinear.

The changes observed in subjects with retinal abnormalities (i.e., subRPE drusen, a hyperreflective lesion in the outer retina) and the feasibility of functional measurements in the affected regions indicate that the technique has the potential to measure functional changes in RPE but needs further exploration in diseased eyes. A more detailed longitudinal study of subjects with varying stages of AMD could provide a quantitative assessment of the change in NIRAF lifetime with disease progression. In addition, NIR-AOFLIO complements the work we previously published on SWAF-AOFLIO,[20] the purpose of the latter being to understand the various changes in autofluorescence signals in RPE and to monitor the alterations in RPE composition of lipofuscin, melanin, and melano-lipofuscin.

Conclusions

Combining adaptive optics with fluorescence lifetime imaging using NIR excitation to visualize the human RPE cellular mosaic in vivo is a valuable tool with good repeatability for the detection of alterations in RPE composition. Consistent cellular-resolved RPE images at foveal and parafoveal locations observed with NIRAF imaging, along with better patient comfort, allow for transition to the clinic. Observed signal in only the pigmented mouse extract indicates that the fluorescence signal we capture at near-infrared excitation comes predominantly from melanin. Variations observed across the retina in a subject with intermediate AMD suggest NIR-AOFLIO can act as a functional biomarker for in vivo monitoring of early and intermediate alterations in retinal health.

Acknowledgments

The authors thank Ethan Rossi for sharing the software used for automatic pinhole alignment and subject alignment target in this study and for conversations regarding the photon collection improvement techniques for infrared autofluorescence imaging to improve the signal to noise.

Supported by the National Institutes of Health Grants RO1 EY032116, P30 EY001319, and RO1EY012951 and by an unrestricted grant to the University of Rochester Department of Ophthalmology from Research to Prevent Blindness, New York, New York.

Disclosure: **K. Kunala**, None; **J.A.H. Tang**, None; **K.E. Bowles Johnson**, None; **K.T. Huynh**, None; **K. Parkins**, University of Rochester (P); **H.-J. Kim**, None; **Q. Yang**, University of Rochester (P), Canon Inc. (P), Montana State University (P); **J.R. Sparrow**, None; **J.J. Hunter**, University of Rochester (P)

References

1. Strauss O. The retinal pigment epithelium in visual function. *Physiol Rev*. 2005;85(3):845–881.
2. Sparrow JR, Hicks D, Hamel CP. The retinal pigment epithelium in health and disease. *Curr Mol Med*. 2010;10(9):802–823.
3. Delori FC, Dorey CK, Staurenghi G, et al. In vivo fluorescence of the ocular fundus exhibits retinal pigment epithelium lipofuscin characteristics. *Invest Ophthalmol Vis Sci*. 1995;36(3):718–729.
4. von Ruckmann A, Fitzke FW, Bird AC. Distribution of fundus autofluorescence with a scanning laser ophthalmoscope. *Br J Ophthalmol*. 1995;79(5):407–412.
5. Keilhauer CN, Delori FC. Near-infrared autofluorescence imaging of the fundus: visualization of ocular melanin. *Invest Ophthalmol Vis Sci*. 2006;47(8):3556–3564.
6. Duncker T, Marsiglia M, Lee W, et al. Correlations among near-infrared and short-wavelength autofluorescence and spectral-domain optical coherence tomography in recessive Stargardt disease. *Invest Ophthalmol Vis Sci*. 2014;55(12):8134–8143.
7. Schmitz-Valckenberg S, Pfau M, Fleckenstein M, et al. Fundus autofluorescence imaging. *Prog Retin Eye Res*. 2021;81:100893.
8. Dysli C, Wolf S, Hatz K, Zinkernagel MS. Fluorescence lifetime imaging in Stargardt disease: potential marker for disease progression. *Invest Ophthalmol Vis Sci*. 2016;57(3):832–841.
9. Vitale AS, Sauer L, Modersitzki NK, Bernstein PS. Fluorescence lifetime imaging ophthalmoscopy (FLIO) in patients with choroideremia. *Transl Vis Sci Technol*. 2020;9(10):33.
10. Hammer M, Jakob-Girbig J, Schwanengel L, et al. Progressive dysmorphia of retinal pigment epithelium in age-related macular degeneration investigated by fluorescence lifetime imaging. *Invest Ophthalmol Vis Sci*. 2021;62(12):2.
11. Goerdt L, Sauer L, Vitale AS, et al. Comparing fluorescence lifetime imaging ophthalmoscopy in atrophic areas of retinal diseases. *Transl Vis Sci Technol*. 2021;10(7):11.

12. Sauer L, Vitale AS, Modersitzki NK, Bernstein PS. Fluorescence lifetime imaging ophthalmoscopy: autofluorescence imaging and beyond. *Eye (Lond)*. 2021;35(1):93–109.
13. Sauer L, Gensure RH, Andersen KM, et al. Patterns of fundus autofluorescence lifetimes in eyes of individuals with nonexudative age-related macular degeneration. *Invest Ophthalmol Vis Sci*. 2018;59(4):AMD65–AMD77.
14. Schwanengel LS, Weber S, Simon R, et al. Changes in drusen-associated autofluorescence over time observed by fluorescence lifetime imaging ophthalmoscopy in age-related macular degeneration. *Acta Ophthalmol*. 2023;101(2):e154–e166.
15. Dysli C, Fink R, Wolf S, Zinkernagel MS. Fluorescence lifetimes of drusen in age-related macular degeneration. *Invest Ophthalmol Vis Sci*. 2017;58(11):4856–4862.
16. Sauer L, Vitale AS, Milliken CM, et al. Autofluorescence lifetimes measured with fluorescence lifetime imaging ophthalmoscopy (FLIO) are affected by age, but not by pigmentation or gender. *Transl Vis Sci Technol*. 2020;9(9):2.
17. Sauer L, Schweitzer D, Ramm L, et al. Impact of macular pigment on fundus autofluorescence lifetimes. *Invest Ophthalmol Vis Sci*. 2015;56(8):4668–4679.
18. Dysli C, Wolf S, Berezin MY, et al. Fluorescence lifetime imaging ophthalmoscopy. *Prog Retin Eye Res*. 2017;60:120–143.
19. Schweitzer D, Deutsch L, Klemm M, et al. Fluorescence lifetime imaging ophthalmoscopy in type 2 diabetic patients who have no signs of diabetic retinopathy. *J Biomed Opt*. 2015;20(6):61106.
20. Tang JAH, Granger CE, Kunala K, et al. Adaptive optics fluorescence lifetime imaging ophthalmoscopy of in vivo human retinal pigment epithelium. *Biomed Opt Express*. 2022;13(3):1737–1754.
21. Cideciyan AV, Swider M, Aleman TS, et al. Reduced-illuminance autofluorescence imaging in ABCA4-associated retinal degenerations. *J Opt Soc Am A Opt Image Sci Vis*. 2007;24(5):1457–1467.
22. Greenstein VC, Schuman AD, Lee W, et al. Near-infrared autofluorescence: its relationship to short-wavelength autofluorescence and optical coherence tomography in recessive Stargardt disease. *Invest Ophthalmol Vis Sci*. 2015;56(5):3226–3234.
23. Granger CE, Yang Q, Song H, et al. Human retinal pigment epithelium: in vivo cell morphometry, multispectral autofluorescence, and relationship to cone mosaic. *Invest Ophthalmol Vis Sci*. 2018;59(15):5705–5716.
24. Stringham JM, Fuld K, Wenzel AJ. Action spectrum for photophobia. *J Opt Soc Am A Opt Image Sci Vis*. 2003;20(10):1852–1858.
25. Bullough JD. Spectral sensitivity for extrafoveal discomfort glare. *J Modern Opt*. 2009;56(13):1518–1522.
26. Tam J, Liu J, Dubra A, Fariss R. In vivo imaging of the human retinal pigment epithelial mosaic using adaptive optics enhanced indocyanine green ophthalmoscopy. *Invest Ophthalmol Vis Sci*. 2016;57(10):4376–4384.
27. Grieve K, Gofas-Salas E, Ferguson RD, et al. In vivo near-infrared autofluorescence imaging of retinal pigment epithelial cells with 757 nm excitation. *Biomed Opt Express*. 2018;9(12):5946–5961.
28. Wing GL, Blanchard GC, Weiter JJ. The topography and age relationship of lipofuscin concentration in the retinal pigment epithelium. *Invest Ophthalmol Vis Sci*. 1978;17(7):601–607.
29. Weiter JJ, Delori FC, Wing GL, Fitch KA. Retinal pigment epithelial lipofuscin and melanin and choroidal melanin in human eyes. *Invest Ophthalmol Vis Sci*. 1986;27(2):145–152.
30. Snodderly DM, Brown PK, Delori FC, Auran JD. The macular pigment. I. Absorbance spectra, localization, and discrimination from other yellow pigments in primate retinas. *Invest Ophthalmol Vis Sci*. 1984;25(6):660–673.
31. Bone RA, Landrum JT, Cains A. Optical density spectra of the macular pigment in vivo and in vitro. *Vis Res*. 1992;32(1):105–110.
32. Davis MD, Gangnon RE, Lee LY, et al. The Age-Related Eye Disease Study severity scale for age-related macular degeneration: AREDS Report No. 17. *Arch Ophthalmol*. 2005;123(11):1484–1498.
33. Huang G, Qi X, Chui TY, Zhong Z, Burns SA. A clinical planning module for adaptive optics SLO imaging. *Optom Vis Sci*. 2012;89(5):593–601.
34. Rossi EA, Rangel-Fonseca P, Parkins K, et al. In vivo imaging of retinal pigment epithelium cells in age related macular degeneration. *Biomed Opt Express*. 2013;4(11):2527–2539.
35. Taubitz T, Fang Y, Biesemeier A, Julien-Schraermeyer S, Schraermeyer U. Age, lipofuscin and melanin oxidation affect fundus near-infrared autofluorescence. *EBioMedicine*. 2019;48:592–604.
36. Yang Q, Hunter J, Parkins K. Microscopy imaging system and methods, US patent Application (Pub. No.: US20230022632A1), 2023, https://patents.google.com/patent/US20230022632A1/en.
37. Nasser M, Meller A. Lifetime-based analysis of binary fluorophores mixtures in the low photon count limit. *iScience*. 2022;25(1):103554.
38. Becker W. *The bh TCSPC Handbook*. 10th ed. 2023. Available on www.becker-hickl.com. Accessed August 01, 2023.
39. Malacrida L, Ranjit S, Jameson DM, Gratton E. The phasor plot: a universal circle to advance fluorescence lifetime analysis and interpretation. *Annu Rev Biophys*. 2021;50:575–593.
40. Digman MA, Caiolfa VR, Zamai M, Gratton E. The phasor approach to fluorescence lifetime imaging analysis. *Biophys J*. 2008;94(2):L14–L16.
41. Stringari C, Cinquin A, Cinquin O, et al. Phasor approach to fluorescence lifetime microscopy distinguishes different metabolic states of germ cells in a live tissue. *Proc Natl Acad Sci USA*. 2011;108(33):13582–13587.
42. Ince C, Coremans JM, Bruining HA. In vivo NADH fluorescence. *Adv Exp Med Biol*. 1992;317:277–296.
43. Kane MA, Napoli JL. Quantification of endogenous retinoids. *Methods Mol Biol*. 2010;652:1–54.
44. Deyl Z, Macek K, Adam M, Vancikova O. Studies on the chemical nature of elastin fluorescence. *Biochim Biophys Acta*. 1980;625(2):248–254.
45. Landrum JT, Bone RA. Lutein, zeaxanthin, and the macular pigment. *Arch Biochem Biophys*. 2001;385(1):28–40.
46. Tang JAH. Characterizing and identifying the fluorescence lifetime of the in vivo human RPE cellular mosaic. The Institute of Optics. University of Rochester ProQuest Dissertations Publishing: University of Rochester; 2023.
47. Kim HJ, Sparrow JR. Novel bisretinoids of human retina are lyso alkyl ether glycerophosphoethanolamine-bearing A2PE species. *J Lipid Res*. 2018;59(9):1620–1629.
48. Kim HJ, Zhao J, Sparrow JR. Vitamin A aldehyde-taurine adduct and the visual cycle. *Proc Natl Acad Sci USA*. 2020;117(40):24867–24875.
49. Kim SR, Fishkin N, Kong J, et al. Rpe65 Leu450Met variant is associated with reduced levels of the retinal pigment epithelium lipofuscin fluorophores A2E and iso-A2E. *Proc Natl Acad Sci USA*. 2004;101(32):11668–11672.
50. Masella BD, Williams DR, Fischer WS, Rossi EA, Hunter JJ. Long-term reduction in infrared autofluorescence caused by infrared light below the maximum permissible exposure. *Invest Ophthalmol Vis Sci*. 2014;55(6):3929–3938.

Investigative Ophthalmology & Visual Science

51. Liu T, Jung H, Liu J, Droettboom M, Tam J. Noninvasive near infrared autofluorescence imaging of retinal pigment epithelial cells in the human retina using adaptive optics. *Biomed Opt Express*. 2017;8(10):4348–4360.
52. Laforest T, Kunzi M, Kowalczuk L, et al. Transscleral optical phase imaging of the human retina. *Nat Photonics*. 2020;14(7):439–445.
53. Bermond K, von der Emde L, Tarau IS, et al. Autofluorescent organelles within the retinal pigment epithelium in human donor eyes with and without age-related macular degeneration. *Invest Ophthalmol Vis Sci*. 2022;63(1):23.
54. Bermond K, Wobbe C, Tarau IS, et al. Autofluorescent granules of the human retinal pigment epithelium: phenotypes, intracellular distribution, and age-related topography. *Invest Ophthalmol Vis Sci*. 2020;61(5):35.
55. Lu R, Aguilera N, Liu T, et al. In-vivo sub-diffraction adaptive optics imaging of photoreceptors in the human eye with annular pupil illumination and sub-Airy detection. *Optica*. 2021;8(3):333–343.
56. Jacques SL. Optical properties of biological tissues: a review. *Phys Med Biol*. 2013;58(11):R37–R61.
57. van de Kraats J, van Norren D. Optical density of the aging human ocular media in the visible and the UV. *J Opt Soc Am A Opt Image Sci Vis*. 2007;24(7):1842–1857.
58. Paavo M, Zhao J, Kim HJ, et al. Mutations in GPR143/OA1 and ABCA4 inform interpretations of short-wavelength and near-infrared fundus autofluorescence. *Invest Ophthalmol Vis Sci*. 2018;59(6):2459–2469.
59. Riesz J, Gilmore J, Meredith P. Quantitative scattering of melanin solutions. *Biophys J*. 2006;90(11):4137–4144.
60. Ueda K, Zhao J, Kim HJ, Sparrow JR. Photodegradation of retinal bisretinoids in mouse models and implications for macular degeneration. *Proc Natl Acad Sci USA*. 2016;113(25):6904–6909.
61. Dimitrow E, Riemann I, Ehlers A, et al. Spectral fluorescence lifetime detection and selective melanin imaging by multiphoton laser tomography for melanoma diagnosis. *Exp Dermatol*. 2009;18(6):509–515.
62. Dancik Y, Favre A, Loy CJ, Zvyagin AV, Roberts MS. Use of multiphoton tomography and fluorescence lifetime imaging to investigate skin pigmentation in vivo. *J Biomed Opt*. 2013;18(2):26022.
63. Krasieva TB, Stringari C, Liu F, et al. Two-photon excited fluorescence lifetime imaging and spectroscopy of melanins in vitro and in vivo. *J Biomed Opt*. 2013;18(3):31107.
64. Ehlers A, Riemann I, Stark M, Konig K. Multiphoton fluorescence lifetime imaging of human hair. *Microsc Res Tech*. 2007;70(2):154–161.
65. Sitiwin E, Madigan MC, Gratton E, et al. Shedding light on melanins within in situ human eye melanocytes using 2-photon microscopy profiling techniques. *Sci Rep*. 2019;9(1):18585.
66. Palczewska G, Boguslawski J, Stremplewski P, et al. Noninvasive two-photon optical biopsy of retinal fluorophores. *Proc Natl Acad Sci USA*. 2020;117(36):22532–22543.
67. Lapierre-Landry M, Carroll J, Skala MC. Imaging retinal melanin: a review of current technologies. *J Biol Eng*. 2018;12:29.
68. Durairaj C, Chastain JE, Kompella UB. Intraocular distribution of melanin in human, monkey, rabbit, minipig and dog eyes. *Exp Eye Res*. 2012;98(1):23–27.
69. Konig K. Clinical multiphoton tomography. *J Biophotonics*. 2008;1(1):13–23.
70. Deka C, Lehnert BE, Lehnert NM, et al. Analysis of fluorescence lifetime and quenching of FITC-conjugated antibodies on cells by phase-sensitive flow cytometry. *Cytometry*. 1996;25(3):271–279.
71. Li W, Houston KD, Houston JP. Shifts in the fluorescence lifetime of EGFP during bacterial phagocytosis measured by phase-sensitive flow cytometry. *Sci Rep*. 2017;7:40341.
72. Hu DN, Simon JD, Sarna T. Role of ocular melanin in ophthalmic physiology and pathology. *Photochem Photobiol*. 2008;84(3):639–644.
73. Kayatz P, Thumann G, Luther TT, et al. Oxidation causes melanin fluorescence. *Invest Ophthalmol Vis Sci*. 2001;42(1):241–246.
74. Bartosz Roź˙anowski JMB, Boulton ME, Sarna T, Roź˙anowska M. Human RPE melanosomes protect from photosensitized and iron-mediated oxidation but become pro-oxidant in the presence of iron upon photodegradation. *Invest Ophthalmol Vis Sci*. 2008;49(7):2838–2847.
75. Glickman RD. *Mechanisms of Photo-Oxidative Stress in Retinal Pigment Epithelium: Is Melanin a Photosensitizer?* San Antonio: Texas University Health Science Center; 1998.
76. Wu Y, Yanase E, Feng X, Siegel MM, Sparrow JR. Structural characterization of bisretinoid A2E photocleavage products and implications for age-related macular degeneration. *Proc Natl Acad Sci USA*. 2010;107(16):7275–7280.
77. Rudolf M, Vogt SD, Curcio CA, et al. Histologic basis of variations in retinal pigment epithelium autofluorescence in eyes with geographic atrophy. *Ophthalmology*. 2013;120(4):821–828.
78. Huynh KT, Walters S, Foley EK, Hunter JJ. Separate lifetime signatures of macaque S cones, M/L cones, and rods observed with adaptive optics fluorescence lifetime ophthalmoscopy. *Sci Rep*. 2023;13(1):2456.

Investigative Ophthalmology & Visual Science